Contact Engineering for High-Performance N-Type 2D Semiconductor Transistors

Y. Lin[1,2], P.-C. Shen[1,3], C. Su[2], A.-S. Chou[4,5], T. Wu[6], C.-C. Cheng[4], J.-H. Park[1], M.-H. Chiu[1], A.-Y. Lu[1], H.-L. Tang[1], M. M. Tavakoli[1], G. Pitner[6], X. Ji[1], C. McGahan[7], X. Wang[8], Z. Cai[1], N. Mao[1], J. Wang[1], Y. Wang[9], W. Tisdale[1], X. Ling[8], K. E. Aidala[7], V. Tung[9], J. Li[1], A. Zettl[2], C.-I. Wu[5], Jing Guo[11], H. Wang[6], J. Bokor[2], T. Palacios[1], L.-J. Li[4,12], J. Kong[1]
[1]Massachussetts Institute of Technology, Cambridge, MA, USA, email: pcshenc@tsmc.com; jingkong@mit.edu
[2]University of California, Berkeley, CA, USA, email: yxlin@berkeley.edu
[3]TSMC, Hsinchu, Taiwan [4]Corporate Research, TSMC, Hsinchu, Taiwan [5]National Taiwan University, Taipei, Taiwan
[6]Corporate Research, TSMC, San Jose, CA, USA [7]Mount Holyoke College, Hadley, MA, USA
[8]Boston University, Boston, MA, USA [9]Tsinghua University, Beijing, China
[10]King Abdullah University of Science & Technology, Thuwal, Saudi Arabia
[11]University of Florida, Gainesville, FL, USA [12]University of Hong Kong, Hong Kong, China

2021 IEEE International Electron Devices Meeting (IEDM) | 978-1-6654-2572-8/21/$31.00 ©2021 IEEE | DOI: 10.1109/IEDM19574.2021.9720668

***Abstract*— Two-dimensional (2D) semiconductors are expected to have exceptional properties for ultimately scaled transistors, but forming ohmic contact to them has been challenging, which tremendously limit the transistor performance. In this paper, we review the recent research progress on the elimination of different gap-state pinning effects, including defect-induced gap states (DIGS) and metal-induced gap states (MIGS). Specifically, an oxygen passivation method and a semimetallic contact technology were developed to reduce the DIGS and MIGS, respectively. Based on these approaches, much improved contact resistance and on-state current were observed. Key device metrics were extracted on these high-performance transistors, which reveals future directions for further improving the device performance.

I. Introduction

2D semiconductors have been envisioned as promising candidates as channel materials for future post-silicon transistor technologies [1], due to their preserved carrier transport properties and great gate control efficiencies at the ultimate scaling limit. A major bottleneck that has been restricting the transistor performance made with monolayer (1L) transition metal dichalcogenides (TMDs), such as MoS_2, WS_2 and WSe_2, is the large Schottky barrier (SB) and the large contact resistance at the metal-2D semiconductor interface. Such a large SB is fundamentally limited by the gap-state pinning effects. There are two major types of gap-state pinning effects: DIGS and MIGS. Previous studies have demonstrated reduction of these gap states and improvement of the contact resistance (R_C), through metal work function engineering [2, 3], electrostatics engineering [4], and interface/interfacial layer engineering [5-8]. In this paper, we report our recent development of new contact engineering approaches, including oxygen-incorporated chemical vapor deposition (O-CVD) and semimetallic contact [9], to reduce the DIGS and MIGS, respectively, which gives rise to much improved R_C and on-state current (I_{ON}) of field effect transistors (FETs) made with 1L TMDs. We further extracted key device metrics of these high-performance 1L TMD FETs, and investigated the effects of different TMDs, different substrates, as well as short-channel effects. Finally, our device technologies are benchmarked, which can help identify both the promises and challenges of 2D-semiconductor-based transistor technologies.

II. Healing of DIGS via O-CVD

The first approach is to passivate the sulfur vacancies (V_S) with oxygen, which eliminates the DIGS-induced SB (Fig. 1). To form stable oxygen bonding to the V_S, oxygen is introduced during the chemical vapor deposition (referred to as O-CVD). Three types of 1L MoS_2 are investigated: MoS_2 grown with oxygen (O-MoS_2), MoS_2 grown in a sulfur-mild condition (SM-MoS_2), and MoS_2 grown in a sulfur-excess condition (SE-MoS_2). Optical microscopic images are shown in the insets of Fig. 2a. I_D-V_{GS} characteristics (Fig. 2a) indicates a less n-type doping of the O-MoS_2 sample. The energy barrier extracted from the Arrhenius plots for the three types of samples are shown in Fig. 2b, from which we can extract the SB height Φ_{SB} at the flatband to be 40, 100, and 200 meV for O-, SM-, and SE-MoS_2, respectively. The much lower SB height for the O-MoS_2 sample leads to 3 times improvement of the R_C, which is extracted to be around 1 kΩ·μm from the transfer length method (TLM), shown in Fig. 2c and d.

The trends observed above can be understood by the efficient passivation of V_S because of the oxygen incorporation. Fig. 3 displays the local density of states (LDOS) of V_S-MoS_2 and O-MoS_2 calculated by density-functional theory (DFT) method. There are substantial donor states within the bandgap of MoS_2 for the V_S-MoS_2 (corresponding to SE- and SM-MoS_2 samples), while these V_S-related deep donor states are replaced by very shallow acceptor states for the O-MoS_2 sample.

Besides the improved SB height, another outcome of the passivation of V_S is the reduced n-type doping, which can be substantiated by shift of the threshold voltage (V_T) in Fig. 2a, as well as the shifts of the A_{1g} Raman mode (Fig. 4a) and the Mo 3d peaks in the X-ray photoemission spectra (XPS, Fig. 4b). The work function obtained from DFT and from electric force microscope (EFM) measurements also indicate a ~300 meV down-shift of the Fermi level (E_F) in O-MoS_2 as compared to

V_S-MoS_2 (Fig. 4c). All of these are consistent with our theoretical understanding.

III. Reduction of MIGS via Semimetal Contact

The second approach is to suppress the MIGS through a semimetallic contact, such as Bi. The low DOS at the charge neutrality point (CNP) of Bi can greatly reduce the generation of MIGS when in contact with MoS_2 (Fig. 5). The CNP happens to align with the conduction band minimum (CBM) of MoS_2, which eliminates the CB-contributed MIGS, leading to a negligible Φ_{SB}. Fig. 6 summarizes the key device characteristics of Bi-contacted 1L MoS_2: (1) the extracted R_C is as low as 130 Ω·μm, independent of the carrier density (n_{2D}) in the MoS_2 channel; (2) the Φ_{SB} is negligible, as compared to a ~100 meV of Φ_{SB} for the conventional Ni-contacted device.

To support our understanding about the improved R_C, simulations are performed using DFT (Fig. 7). MIGS are extremely small at the Bi-MoS_2 interface, and the E_F at thermal equilibrium is slightly above the CBM of MoS_2 (Fig. 7a). The small contact resistivity (ρ_C) originates from the tunneling barrier at the van der Waals (vdW) gap, with a barrier height (Φ_t) of 3.6 eV and an effective barrier width (w_t) of 1.66 Å, corresponding to a ρ_C of 1.8×10^{-9} Ω·cm^2, and a R_C of 130 Ω·μm, in very good agreement with the experimentally extracted values (Fig. 7c). In addition, the transfer length (L_T) is extracted to be only 7 nm. Both R_C and L_T are much better than previously reported contact technologies.

The degenerate-state of MoS_2 when in contact with Bi can be further evidenced by the shifts of A_{1g} Raman mode and the XPS Mo 3d peaks as shown in Fig. 8.

IV. Performance Evaluation and Projection

With the aforementioned strategies, especially the semimetallic contact, exceptional performance is obtained on FETs made with various 1L TMDs on different back-gate dielectrics. Typical *I-V* characteristics for Bi-contacted 1L MoS_2, WS_2, and WSe_2 on 100-nm-SiN_x back-gate dielectric, and Bi-contacted MoS_2 on 100-nm-SiN_x and on 5-nm HfO_2 back-gate dielectrics are plotted in black dots in Fig. 9 and Fig. 10 (channel length L = 100 nm), respectively. I_{ON} of >300 μA/μm are achieved. The I_{ON} can be further enhanced to 1135 μA/μm as L is scaled down to 35 nm (Fig. 11), which is the record-high value for TMD FETs. The theoretical limit of the Bi-contacted 1L MoS_2 FET is projected by solving the non-equilibrium Green's function (NEGF) transport equation self-consistently with a 2D Poisson's equation with the contact DOS from DFT calculation (Fig. 12). We first calibrate the model to the experimental data with scattering and then estimate the theoretical limit under ballistic transport. For a L = 20 nm FET with 5 nm HfO_2 gate dielectric, I_{ON} = 2153 μA/μm (at V_{DS} = 1 V).

To extract more information about the device characteristics, a virtual source compact model is used to fit to the experimental *I-V* data. The solid lines in color in Fig. 10-12 are the fitted curves by the compact model, in good agreement with the experimental results. The distributions of V_T, R_C, effective mobility (μ_{eff}), and saturation velocity (v_{sat}) extracted from *I-V* characteristics of tens of devices made with MoS_2, WS_2 and WSe_2 are summarized in Fig. 13. The major findings are: (1) R_C for all three materials are well below 1 kΩ·μm, although WS_2 and WSe_2 devices have slightly greater R_C. This can be explained by the higher CBM of these two materials. (2) μ_{eff} and v_{sat} of MoS_2 are also better than WS_2, and WSe_2, whereas more n-type doping is observed in MoS_2 (more negative V_T).

Fig. 14 summarizes the statistics of μ_{eff} and v_{sat} of MoS_2 devices on different substrates. It is clearly seen that both μ_{eff} and v_{sat} are significantly higher for the MoS_2 on SiN_x devices. Such a discrepancy may be related to the larger optical phonon energies of nitrides than those of oxides, which induces less remote optical phonon scattering in the 1L TMD channel at room temperature.

The dependence of the subthreshold swing (SS) and drain-induced barrier lowering (DIBL) on the channel length of the Bi-contacted MoS_2 on 5 nm HfO_2 gate dielectrics are shown in Fig. 15. Exceptional DIBL of 10-60 mV/V are observed, whereas the SS is 145 mV/dec for the long-channel device (L = 300 nm), which degrades to 220 mV/dec for the short-channel device (L = 100 nm). The SS can be improved by either better design of the gate stacks (such as dual gate, or surrounding gate), or carefully engineering of the interfaces and trap states.

Finally, we benchmark the I_{ON} (with V_{DS} = 1 V) and SS among our work and previous reports, as summarized in Fig. 16. Our reported I_{ON} values are among the best reported values[4, 9-11]. There is still a lot of room to further improve the gate stacks for a better SS value. The NEGF simulated result is also shown as a theoretical limit of this technology. Fig. 17 summarizes reported R_C as functions of material thickness and carrier density [9]. Our Bi-contact technologies are several times better than previous results, on par with silicon technologies, and approaching the quantum limit.

Acknowledgment

This work is supported by NSF E3S Center 0939514, ARO MIT-ISN W911NF-18-2-0048, ONR MURI N00014-16-1-2921, NSF DMR-1839098, ARO W911NF-18-1-0431, DOE DE-AC02- 05-CH11231, DOE DE-SC0020042, MOST 109-2622-8-002-003, TSMC JDP, NSF-DMR 1708970, SRC S4994.

References

[1] D. Akinwande, *et al.*, *Nature,* vol. 573, pp. 507-518, 2019.
[2] S. Das, *et al.*, *Nano Letters,* vol. 13, pp. 100-105, 2013.
[3] S. Chuang, *et al.*, *Nano Letters,* vol. 14, pp. 1337-1342, 2014.
[4] C. J. McClellan, *et al.*, *ACS nano,* vol. 15, pp. 1587-1596, 2021.
[5] X. Cui, *et al.*, *Nano letters,* vol. 17, pp. 4781-4786, 2017.
[6] C. D. English, *et al.*, *Nano Letters,* vol. 16, pp. 3824-3830, 2016.
[7] Y. Wang, *et al.*, *Nature,* vol. 568, pp. 70-74, 2019.
[8] Y. Liu, *et al.*, *Nature,* vol. 557, pp. 696-700, 2018.
[9] P.-C. Shen, *et al.*, *Nature,* vol. 593, pp. 211-217, 2021.
[10] A. S. Chou, *et al.*, *VLSI* 2020, p. 9265040.
[11] Q. Smets, *et al.*, *IEDM* 2019, pp. 23.2. 1-23.2. 4.
[12] C. J. Dorow, *et al.*, VLSI 2021, p. T2.3.
[13] A. D. Daus, *et al.*, *Nat. Electr*. vol. 4, pp. 495-501, 2021

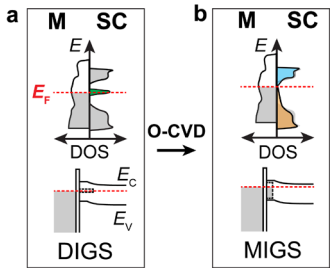

Fig. 1. DIGS pinning mechanisms and solutions. Density of states (DOS) and band diagrams at the metal (M) – semiconductor (SC) junctions in cases of (a) DIGS due to chalcogen vacancies; (b) MIGS, where DIGS is eliminated after O-passivation.

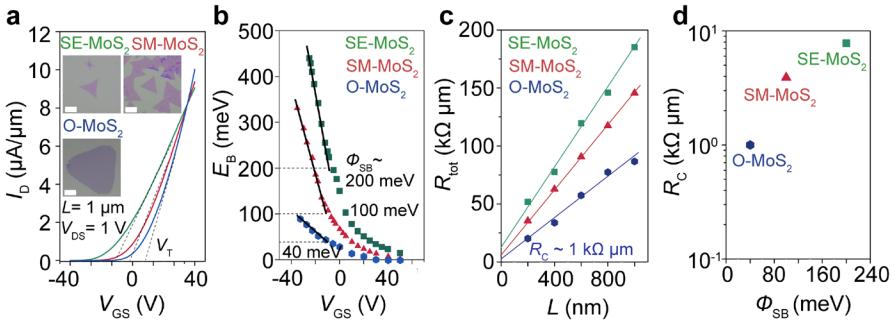

Fig. 2. Electrical characterization of O-MoS_2 transistor and its metal contact. (a) I_D-V_{GS} characteristics of SE-MoS_2 (green), SM-MoS_2 (red), and O-MoS_2 (blue) FETs with Ni contacts on a 285-nm-SiO_2 back-gate dielectric. (b) Energy barrier E_B versus V_{GS} for the three types of samples. (c) TLM for the three types of samples. (d) Extracted R_C versus Φ_{SB}.

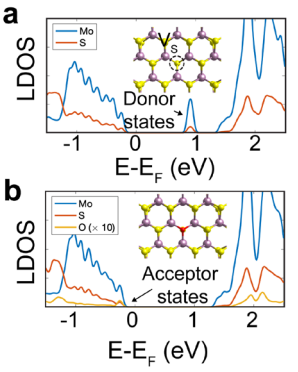

Fig. 3. DFT calculation of O-MoS_2 (a) LDOS for sulfur vacancy MoS_2. (b) LDOS for O- MoS_2.

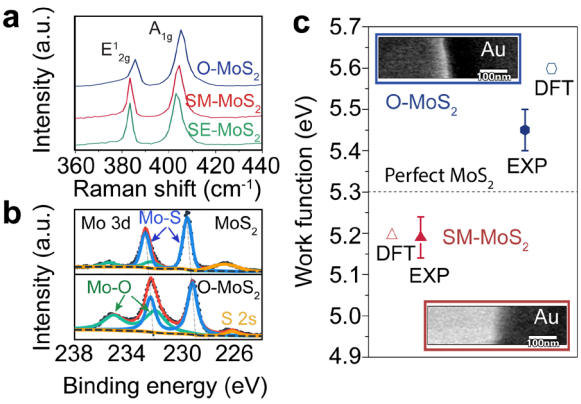

Fig. 4. (a) Raman spectra of the three types of MoS_2. (b) XPS spectra of the three types of MoS_2. (c) Work function measured by EFM and calculated from DFT. The insets are typical EFM images of O-MoS_2 and SM-MoS_2.

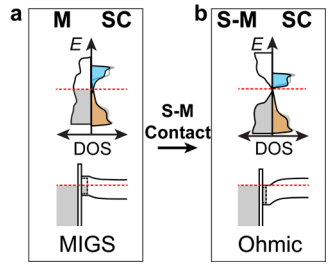

Fig. 5. MIGS pining mechanisms and solutions. DOS and band diagrams in cases of (a) MIGS; (b) ohmic contact where MIGS in TMDs can be reduced by semimetalic (S-M) contact.

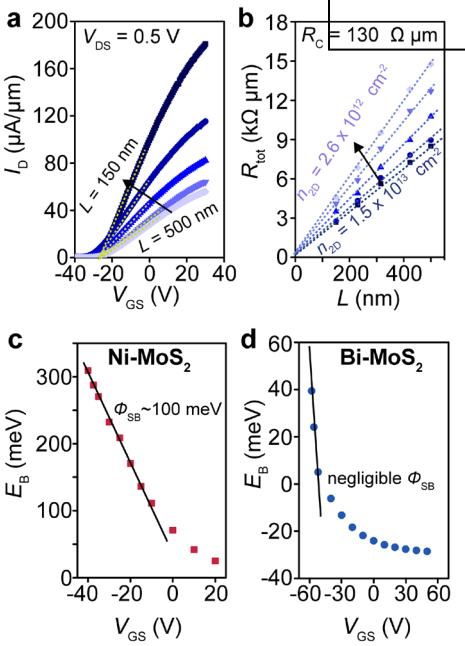

Fig. 6. Electrical characterization of Bi-1L MoS_2 contact. (a) I_D-V_{GS} characteristics of 1L MoS_2 with different channel lengths, L, on a 100-nm-SiN_x back-gate dielectric. (b) TLM with different 2D carrier density, n_{2D}. (c) Energy barrier E_B versus V_{GS} of Ni-1L MoS_2 contact. (d) Energy barrier E_B versus V_{GS} of Bi-1L MoS_2 contact.

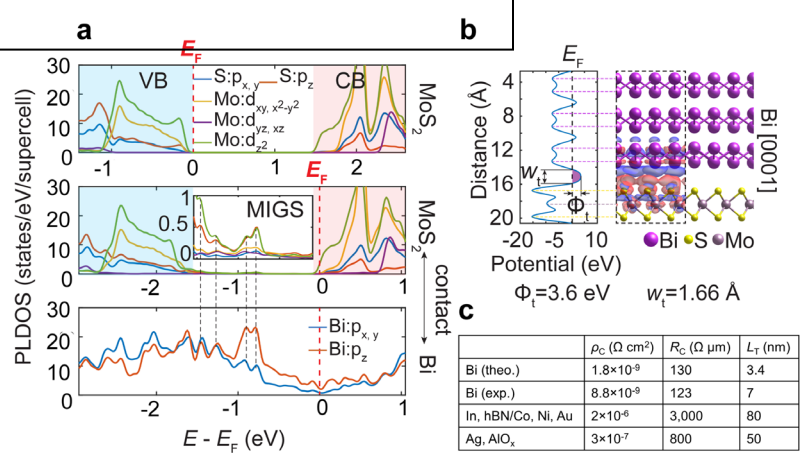

	ρ_C (Ω cm²)	R_C (Ω μm)	L_T (nm)
Bi (theo.)	1.8×10^{-9}	130	3.4
Bi (exp.)	8.8×10^{-9}	123	7
In, hBN/Co, Ni, Au	2×10^{-6}	3,000	80
Ag, AlO_x	3×10^{-7}	800	50

Fig. 7. DFT calculation of Bi/MoS_2 contact. (a) Projected local density of states (PLDOS) for pristine MoS_2 (top), as well as MoS_2 (middle) and Bi (bottom) when they are in contact. The inset is a magnified PLDOS within the bandgap of MoS_2, showing very low MIGS. (b) The side view of Bi–MoS_2 (right), and the corresponding electrostatic potential profile along the vertical direction (left). The differential charge density inside the region of dashed line. (c) Summary of ρ_C, R_C and L_T.

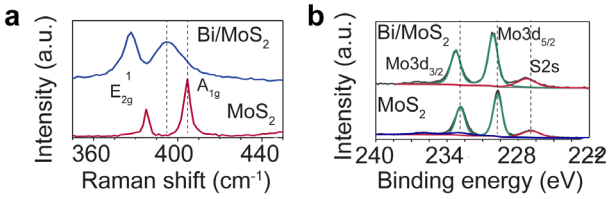

Fig. 8. (a) Raman spectra of Bi/MoS_2 (blue) and MoS_2 (red). (b) XPS spectra of Bi/MoS_2 (top) and MoS_2 (bottom).

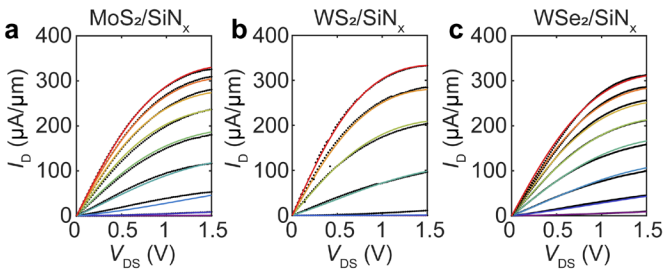

Fig. 9. I_D-V_{DS} characteristics for (a) MoS_2, (b) WS_2, and (c) WSe_2. All devices are fabricated with Bi contacts on 100-nm-SiN_x back-gate dielectrics, with L = 100 nm. V_{DS} ranges are: (a) from -30 V to 50 V; (b) from 0 to 50 V; (c) from -10 to 60V. All of them are with steps of 10 V.

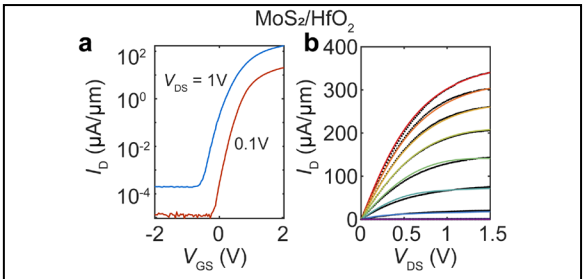

Fig. 10. (a) I_D-V_{GS} and (b) I_D-V_{DS} characteristics for MoS_2, device fabricated with Bi contacts on 5-nm-HfO_2 back-gate dielectrics, with L = 100 nm. In (b), V_{DS} is changed from 0 V to 4 V with steps of 0.5 V.

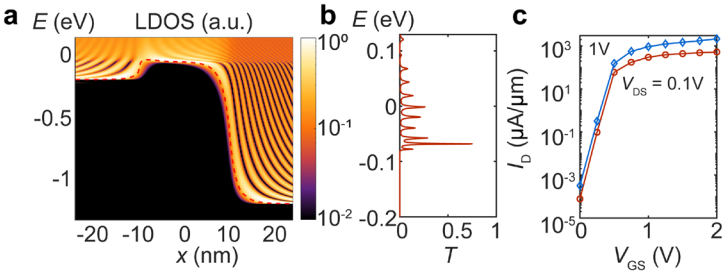

Fig. 12. NEGF simulation results for a MoS_2 FET on 5 nm HfO_2 dielectric with L = 20 nm. (a) Local density of states (LDOS) when V_{GS} = V_{DS} = 1 V. (b) The corresponding transmittance spectrum. (c) Simulated I_D-V_{GS} response.

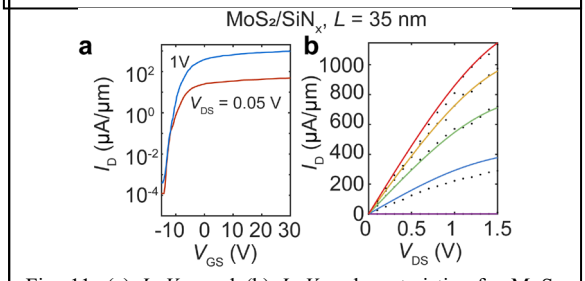

Fig. 11. (a) I_D-V_{GS} and (b) I_D-V_{DS} characteristics for MoS_2, device fabricated with Bi contacts on 100-nm-SiN_x back-gate dielectrics, with L = 100 nm. In (b), V_{DS} is changed from -10 V to 30 V with steps of 10 V.

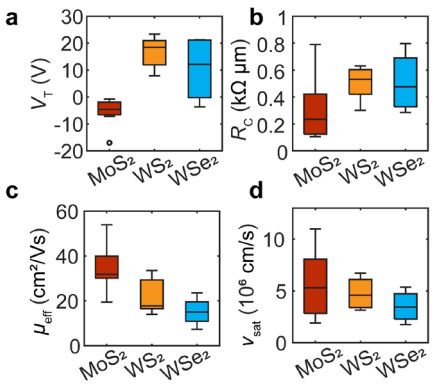

Fig. 13. Comparison of different TMDs in terms of: (a) V_T; (b) R_C; (c) μ_{eff}; and (d) v_{sat}. All parameters are extracted from experimental measurements with the help

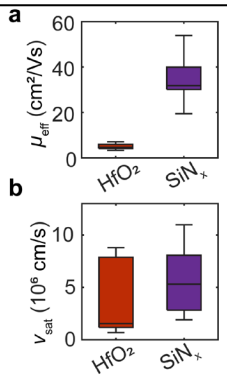

Fig. 14. Comparison of different substrates in terms of: (a) μ_{eff}; and (b) v_{sat}.

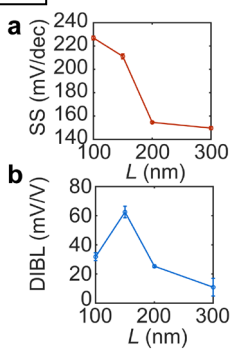

Fig. 15. Channel length dependence of (a) SS, and (DIBL) of MoS_2 transistor with 5 nm HfO_2 back-gate dielectrics

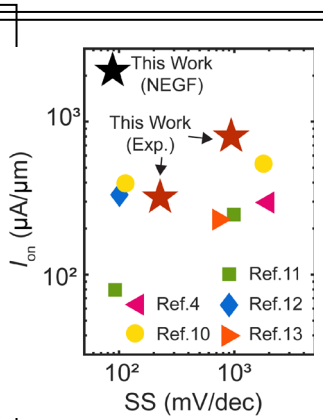

Fig. 16. Benchmark of I_{on} and SS.

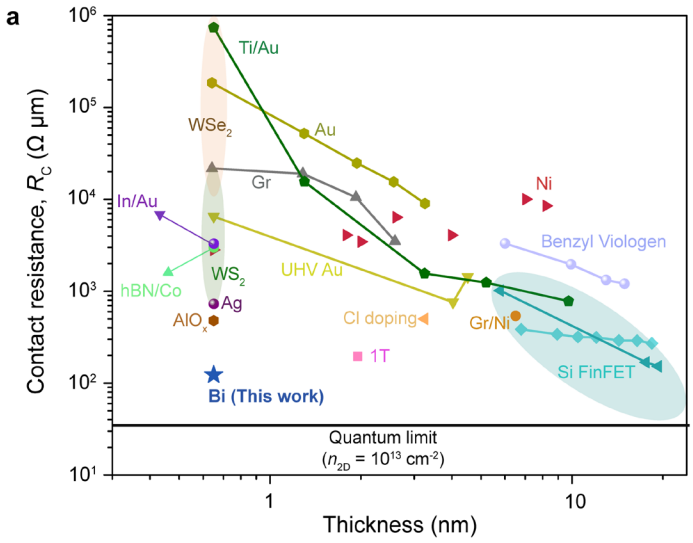

Fig. 17. Benchmark of R_C. (a) R_C versus thickness; (b) R_C versus carrier density [9].